Coherent transport properties of a three-terminal hybrid superconducting interferometer

Vischi, F.; Carrega, M.; Strambini, E.; D'Ambrosio, S.; Bergeret, F. S.; Nazarov, Yu V.; Giazotto, F.

DOI
10.1103/PhysRevB.95.054504

Publication date
2017

Document Version
Final published version

Published in
Physical Review B (Condensed Matter and Materials Physics)

Citation (APA)
Vischi, F., Carrega, M., Strambini, E., D'Ambrosio, S., Bergeret, F. S., Nazarov, Y. V., & Giazotto, F. (2017). Coherent transport properties of a three-terminal hybrid superconducting interferometer. *Physical Review B (Condensed Matter and Materials Physics)*, *95*(5), Article 054504. https://doi.org/10.1103/PhysRevB.95.054504

Coherent transport properties of a three-terminal hybrid superconducting interferometer

F. Vischi,[1,2] M. Carrega,[1] E. Strambini,[1] S. D'Ambrosio,[1] F. S. Bergeret,[3,4] Yu. V. Nazarov,[5] and F. Giazotto[1,*]
[1]*NEST, Istituto Nanoscienze-CNR and Scuola Normale Superiore, I-56127 Pisa, Italy*
[2]*Dipartimento di Fisica, Università di Pisa, I-56127 Pisa, Italy*
[3]*Centro de Fisica de Materiales (CFM-MPC), Centro Mixto CSIC-UPV/EHU, Manuel de Lardizabal 5, E-20018 San Sebastian, Spain*
[4]*Donostia International Physics Center (DIPC), Manuel de Lardizabal 5, E-20018 San Sebastian, Spain*
[5]*Kavli Institute of Nanoscience, Delft University of Technology, Lorentzweg 1, 2628 CJ, Delft, The Netherlands*
(Received 28 November 2016; published 13 February 2017)

We present an exhaustive theoretical analysis of a double-loop Josephson proximity interferometer, such as the one recently realized by Strambini *et al.* for control of the Andreev spectrum via an external magnetic field. This system, called ω-SQUIPT, consists of a T-shaped diffusive normal metal (N) attached to three superconductors (S) forming a double-loop configuration. By using the quasiclassical Green-function formalism, we calculate the local normalized density of states, the Josephson currents through the device, and the dependence of the former on the length of the junction arms, the applied magnetic field, and the S/N interface transparencies. We show that by tuning the fluxes through the double loop, the system undergoes transitions from a gapped to a gapless state. We also evaluate the Josephson currents flowing in the different arms as a function of magnetic fluxes, and we explore the quasiparticle transport by considering a metallic probe tunnel-coupled to the Josephson junction and calculating its I-V characteristics. Finally, we study the performances of the ω-SQUIPT and its potential applications by investigating its electrical and magnetometric properties.

DOI: 10.1103/PhysRevB.95.054504

I. INTRODUCTION

The superconducting quantum interference proximity transistor (SQUIPT) [1] is a new concept of a superconducting interferometer based on the proximity effect [2,3] in a normal (N) metallic nanowire embedded in a superconducting (S) loop. The phase-controlled density of states (DOS) of the proximized nanowire makes the SQUIPT an ideal building block for the realization of heat nanovalves [4] or very sensitive and ultra-low-power dissipation magnetometers [5–8] able to succeed the state-of-the-art SQUID technologies, with particular interest in single-spin detection [9].

The ω-SQUIPT is the natural evolution of standard two-terminal geometry, enriched by a third terminal in the metallic Josephson junction, as sketched in Fig. 1. It is composed of a T-shaped N nanowire proximized by two S loops, encircling two independent magnetic fluxes. The ω-SQUIPT represent a useful tool to explore the nontrivial physics accessible in multiterminal Josephson junctions (JJs), in which the Andreev bound states can cross the Fermi level (zero-energy) [10] to tailor exotic quantum states [11–15], to simulate topological materials able to support Majorana bound states in the case of quasiballistic junctions with strong spin-orbit coupling [12,16], or to implement different kinds of Q-bits [17] or switchers [18]. The first ω-SQUIPT was realized [19] very recently with a diffusive three-terminal JJ. The experiment, in agreement with theoretical expectations, demonstrates that a superconducting-like gapped state is induced in the weak link and nontrivially controlled by an external magnetic field. Moreover, this state can be topologically classified by the winding numbers of the two S loops.

The aim of this work is to address the role of the main experimental parameters of the ω-SQUIPT on the spectral and transport properties. For this purpose, the effects of junction length, the transparency of the SN interfaces, and inelastic scattering are discussed. In addition to the analysis of the quasiparticle density of states, a study of the supercurrent flowing in the different arms of the device is reported. Such coherent transport properties in the ω-SQUIPT can be a mark of topological transitions [11,12].

The paper is organized as follows. The model based on the solution of the Usadel equation [3,20] for the quasiclassical Green-functions formalism is described in Sec. II. The analysis of the local normalized DOS is presented in Sec. III, where we discuss the effect of the length of the proximized metallic junction, of the inelastic scattering, and the transparency of the contact interface. The Josephson and the quasiparticle currents are calculated in Secs. IV and V, respectively. In Sec. VI, we summarize our main findings.

II. MODEL AND GENERAL SETTINGS

The ω-SQUIPT is made of a T-shaped N weak link formed by three diffusive quasi-one-dimensional arms of lengths L_i ($i = L,C,R$), as sketched in Fig. 1. Each of the arms is connected to a superconducting lead S_i with phase φ_i and gap Δ_0. The three superconducting phases are linked by the two magnetic fluxes Φ_L and Φ_R piercing the double loop of the interferometer (see Fig. 1). The properties of the device can be described by using the isotropic quasiclassical retarded Green functions $\hat{g}_i$, which are 2×2 matrices in the Nambu space [21]. In a stationary case, these functions satisfy the Usadel equations in each arm (i) of the ω-SQUIPT [3,20],

$$\partial_x(\hat{g}_i \partial_x \hat{g}_i) + i\frac{(E + i\Gamma_N)}{E_i}[\hat{\tau}_3,\hat{g}_i] = 0, \tag{1}$$

where $\hat{\tau}_3$ is the third Pauli matrix in the Nambu space and x is the normalized spatial coordinate mapping the T-shaped weak link from the center ($x = 0$) to the S/N interface ($x = 1$).

*f.giazotto@sns.it

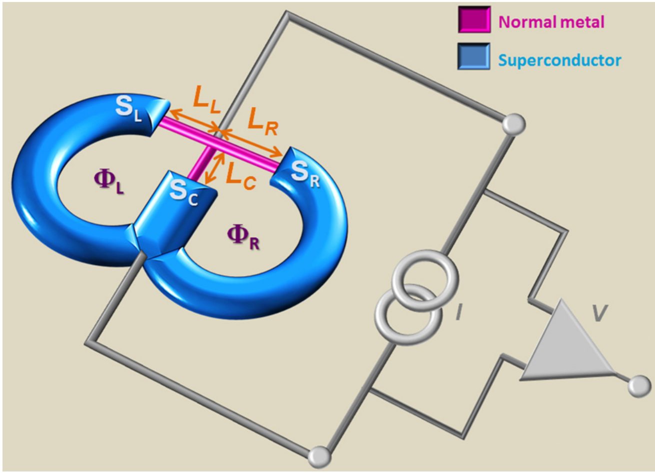

FIG. 1. Scheme of the ω-SQUIPT in a current-biased setup. I is the current flowing through the circuit, and V is the voltage drop across the device. Φ_L and Φ_R represent the magnetic fluxes piercing the left and right loop, respectively. L_L, L_C, and L_R refer to the left, center, and right arms length of the T-shaped normal metal, respectively. Finally, S_L, S_C, and S_R refer to the left, center, and right superconducting leads.

$E_i \equiv \hbar D/L_i^2$ is the (reduced) Thouless energy associated with each arm of the link, and Γ_N is a parameter that takes into account the inelastic processes in the N region. Equation (1) is complemented by the normalization condition

$$\hat{g}_i^2 = \hat{1}, \tag{2}$$

and boundary conditions at the three S/N interfaces and in the middle of the T-shaped junction.

At the S/N interfaces, the Green function has to satisfy the boundary conditions for arbitrary transparency [22,23],

$$r_i\, \hat{g}_i\, \partial_x \hat{g}_i = \frac{2\,[\hat{g}_i,\hat{G}_i]}{4+\tau(\{\hat{g}_i,\hat{G}_i\}-2)}, \tag{3}$$

where τ is the transmission coefficient, the opacity coefficient $r_i = G_{N_i}/G_{B_i}$ is the ratio between the conductance of each arm G_{N_i} and the barrier conductance G_{B_i}, and

$$\hat{G}_i = \frac{1}{\sqrt{(E^R)^2-\Delta_0^2}}\begin{pmatrix} E^R & \Delta_0 e^{i\varphi_i} \\ -\Delta_0 e^{-i\varphi_i} & -E^R \end{pmatrix} \tag{4}$$

is the BCS Green function of the S_i lead [24], $\Delta_0 e^{i\varphi_i}$ is the superconducting order parameter, and $E^R \equiv E + i\Gamma_S$, where Γ_S is the Dynes parameter [25,26]. Neglecting the inductance of the superconducting loops, we can link the two superconducting phase differences to the two magnetic fluxes: $\varphi_L - \varphi_C = 2\pi\Phi_L/\Phi_0$ and $\varphi_R - \varphi_C = -2\pi\Phi_R/\Phi_0$, with $\Phi_0 = h/2e$ the flux quantum (hereafter e indicates the modulus of the electron charge). Notice that for the sake of simplicity in Eq. (3) we have assumed that all the conduction channels at all the interfaces have the same transmission τ and therefore $G_{B_i} = G_0 N_i \tau$, where G_0 is the quantum of conductance and N_i is the number of conducting channels at the ith interface.

In the middle of the T-shaped junction, $x = 0$, we impose the continuity of $\hat{g}_i$:

$$\hat{g}_L(x=0) = \hat{g}_C(x=0) = \hat{g}_R(x=0), \tag{5}$$

and the matrix current conservation

$$\sum_{i=R,C,L} G_{N_i}\, \hat{g}_i\, \partial_x \hat{g}_i\, |_{x=0} = 0. \tag{6}$$

To solve Eqs. (1)–(6), we introduce the Riccati parametrization that parametrizes $\hat{g}_i$ in term of two auxiliary functions $\gamma_i(x,E)$ and $\tilde{\gamma}_i(x,E)$. Therefore, Eqs. (1) and (2) become a system of six coupled differential equations:

$$\begin{aligned} \partial_x^2\gamma_i - \frac{2\tilde{\gamma}_i}{1+\gamma_i\tilde{\gamma}_i}(\partial_x\gamma_i)^2 + 2i\left(\frac{E+i\Gamma_N}{E_i}\right)\gamma_i = 0,\\ \partial_x^2\tilde{\gamma}_i - \frac{2\gamma_i}{1+\gamma_i\tilde{\gamma}_i}(\partial_x\tilde{\gamma}_i)^2 + 2i\left(\frac{E+i\Gamma_N}{E_i}\right)\tilde{\gamma}_i = 0, \end{aligned} \tag{7}$$

with boundary conditions at $x = 0$ [see Eqs. (5) and (6)] (here $i,k \in R,C,L$),

$$\begin{aligned} \gamma_i &= \gamma_k,\\ \tilde{\gamma}_i &= \tilde{\gamma}_k,\\ \sum_i G_{N_i}\frac{\partial_x\gamma_i + (\gamma_i)^2\partial_x\tilde{\gamma}_i}{1+\gamma_i\tilde{\gamma}_i} &= 0,\\ \sum_i G_{N_i}\frac{\partial_x\tilde{\gamma}_i + (\tilde{\gamma}_i)^2\partial_x\gamma_i}{1+\gamma_i\tilde{\gamma}_i} &= 0. \end{aligned} \tag{8}$$

At the S/N interfaces ($x = 1$), the boundary condition in Eq. (3) reads

$$\begin{aligned} &r_i\frac{\partial_x\gamma_i + \gamma_i^2\partial_x\tilde{\gamma}_i}{(1+\gamma_i\tilde{\gamma}_i)^2}\\ &= \frac{(1-\gamma_i\tilde{\gamma}_i)\gamma_i^S - (1-\gamma_i^S\tilde{\gamma}_i^S)\gamma_i}{(1+\gamma_i\tilde{\gamma}_i)(1+\gamma_i^S\tilde{\gamma}_i^S) - \tau(\gamma_i^S-\gamma_i)(\tilde{\gamma}_i^S-\tilde{\gamma}_i)}, \end{aligned} \tag{9}$$

and an analogous equation after substituting γ_i by $\tilde{\gamma}_i$. The functions $\gamma_i^S = \gamma_0 e^{-i\phi_i}$, $\tilde{\gamma}_i^S = -\gamma_0 e^{i\phi_i}$ are the auxiliary functions parametrizing the BCS bulk Green functions, with

$$\gamma_0 = \frac{-\Delta_0}{E + i\Gamma_S + i\sqrt{(\Delta_0)^2 - (E+i\Gamma_S)^2}}. \tag{10}$$

By solving these equations numerically, we obtain the functions γ_i, which determine the DOS, the supercurrent, and the quasiparticle current in the ω-SQUIPT. All these observables are discussed in the next sections.

In the following calculations, we assume a fully symmetric structure, i.e., $L_L = L_C = L_R \equiv L$ and $G_{N_L} = G_{N_C} = G_{N_R} \equiv G_N$; thus, we define a single Thouless energy for the whole junction, $E_{\mathrm{Th}} \equiv \hbar D/(2L)^2 = E_i/4$, to adopt the same energy scale defined in two-terminal geometry. When not explicitly indicated, we will assume ideal interfaces and hence impose the continuity of γ at the S/N interfaces. Only when analyzing the role of the S/N interface resistances will we make use of boundary condition (9).

III. THE DENSITY OF STATES IN THE N REGION

In this section, we investigate the DOS in the T-shaped normal region and its dependence on various parameters. The local normalized DOS in the ith arm of the proximized nanowire is given by

$$N_i(x,E,\Phi_L,\Phi_R) = \frac{1}{2}\,\mathrm{Re}\,\mathrm{Tr}\{\hat{\tau}_3\hat{g}_i\} = \mathrm{Re}\left\{\frac{1-\gamma_i\tilde{\gamma}_i}{1+\gamma_i\tilde{\gamma}_i}\right\}. \quad (11)$$

We start by analyzing the local DOS at the Fermi level in the middle of the T-shaped N wire, $N_F(\Phi_L,\Phi_R) \equiv N_i(x=0, E=0,\Phi_L,\Phi_R)$, as a function of the two fluxes Φ_L and Φ_R through the two loops. Figure 2 shows a typical result for this dependence. We clearly identify gapped (in blue) regions separated by gapless ones (in red). From the top panel to the bottom one, we can notice the effects of the finite quasiparticle lifetime in the superconductor leads (left column) and inelastic scattering in the normal metal (right column), described, respectively, by the parameters Γ_S/Δ_0 and Γ_N/E_{Th}.

It is instructive to note that the density of states precisely at the Fermi energy does not depend on the size of the normal region, unless we assume a significant rate of inelastic scattering Γ_N. In the latter case, the size enters the equations through the ratio Γ_N/E_{Th}.

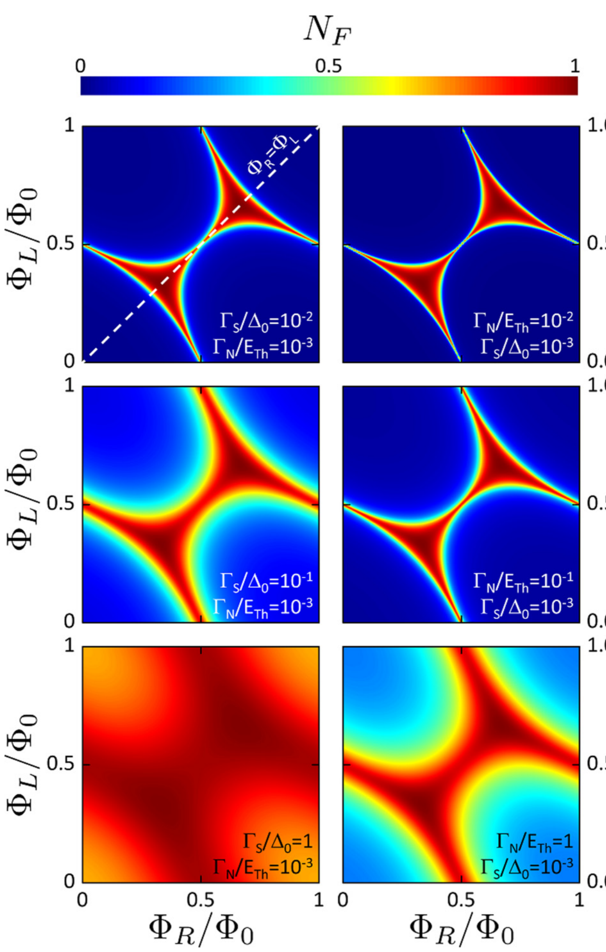

FIG. 2. Evolution of the DOS at the Fermi energy $N_F(\Phi_L,\Phi_R)$ for increasing pair-breaking scattering both in the S leads, Γ_S (left column), and in the N weak link, Γ_N (right column). The values of Γ_N/E_{Th} and Γ_S/Δ_0 are reported in each panel. The weak link is of an intermediate length $E_{\mathrm{Th}}/\Delta_0 = 0.5$ and the S/N interfaces are transparent.

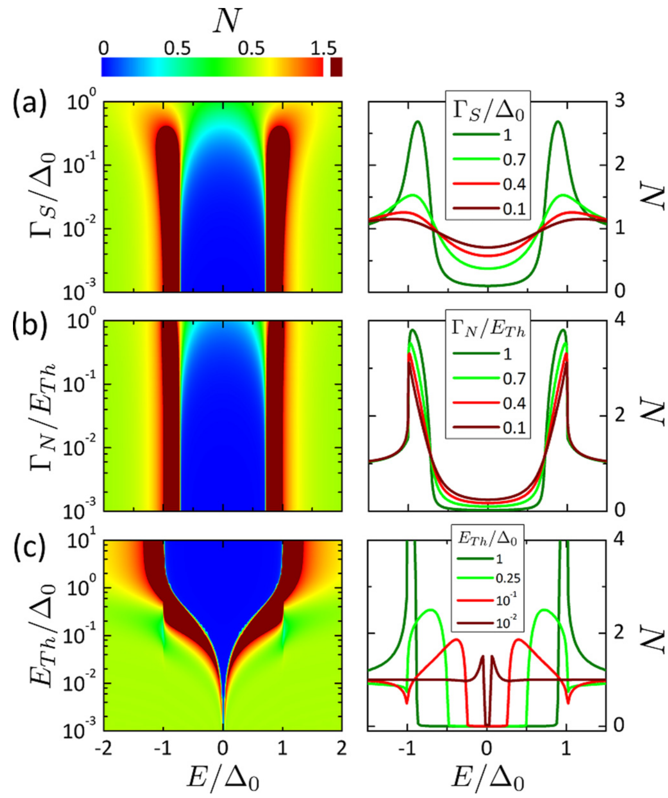

FIG. 3. DOS in the center of the three-terminal junction ($x = 0$) calculated at zero fluxes, $\Phi_L = \Phi_R = 0$. (a) Dependence of the DOS on Γ_S/Δ_0 (fixed $E_{\mathrm{Th}}/\Delta_0 = 0.5$ and $\Gamma_N/E_{\mathrm{Th}} = 10^{-3}$). (b) Dependence of the DOS on Γ_N/E_{Th} (fixed $E_{\mathrm{Th}}/\Delta_0 = 0.5$ and $\Gamma_S/\Delta_0 = 10^{-3}$). (c) Dependence of the DOS on the Thouless energy E_{Th}/Δ_0 (fixed $\Gamma_S = \Gamma_N = 10^{-3}\Delta_0$).

The white dashed line tracks the case of equal fluxes in the two loops, $\Phi_L = \Phi_R \equiv \Phi$, experimentally realizable placing a symmetric ω-SQUIPT in a homogeneous magnetic field. Figure 2 suggests that the gap closes at $\Phi \approx \Phi_0/3$, as confirmed by recent measurements [19]. Interestingly enough, to each gapped region it can be assigned a topological index defined by the pair of numbers obtained by the integration of the superconducting phase gradient over the left and right loop [19]. We note that our results agree well with the recent findings of Ref. [27], where an analytical approach for a multiterminal geometry at the Fermi level has been investigated.

We consider now the DOS at equal fluxes for all energies. In Fig. 3, we compare the detrimental role played by Γ_S, Γ_N, and E_{Th} in the DOS calculated at $\Phi = 0$ for which the proximity effect is maximized. The main common feature is the appearance of an induced minigap Δ_w. As expected, increasing Γ_N or Γ_S causes the smearing of the gapped feature, as one can see in panels (a) and (b) of Fig. 3. The dependence on Thouless energy (then on junction size) is showed in panel (c) of Fig. 3. Similarly to two-terminal geometry, the induced minigap Δ_w decreases with decreasing Thouless energy [28].

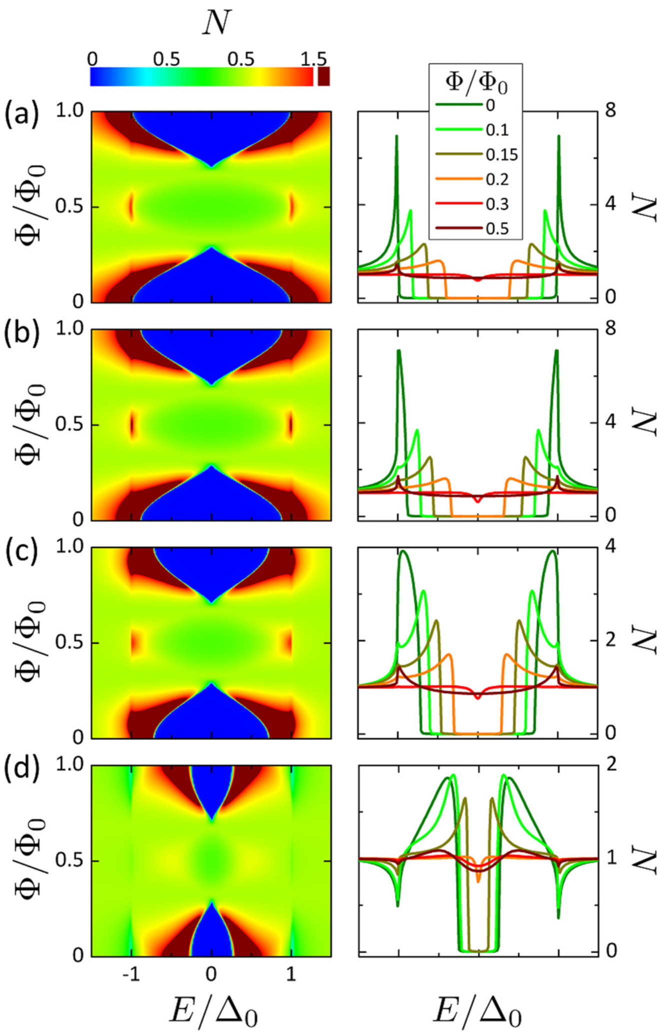

FIG. 4. DOS calculated in the middle of the three-terminal junction ($x = 0$) for equal fluxes $\Phi_L = \Phi_R \equiv \Phi$ with $\Gamma_S = \Gamma_N = 10^{-3}\Delta_0$. Each panel corresponds to a different Thouless energy: (a) $E_{\text{Th}}/\Delta_0 = 5$; (b) $E_{\text{Th}}/\Delta_0 = 1$; (c) $E_{\text{Th}}/\Delta_0 = 0.5$; and (d) $E_{\text{Th}}/\Delta_0 = 0.1$.

In Fig. 4, we illustrate the dependence of the DOS on equal magnetic fluxes $\Phi = \Phi_R = \Phi_L$. Each panel corresponds to a different length. From top to bottom, we explore the behavior of the DOS from short to long junctions, with $E_{\text{Th}}/\Delta_0 = 5, 1, 0.5$, and 0.1, respectively. In the short-junction limit [Fig. 4(a)], our results are in good agreement with those of Ref. [10], obtained within the circuit theory. This limit is achievable for conventional metals in use in nanofabrication at $L \lesssim 100$ nm. Above this limit, the minigap rescales in energy [as observed also in Fig. 3(c)] while the behavior in Φ is practically unaffected. In fact, for all the lengths explored, the induced minigap is modulated by the magnetic flux and disappear in an extended flux interval $1/3 < \Phi/\Phi_0 < 2/3$, repeated with Φ_0 periodicity. This continuous gapless region is the main hallmark of multiterminal JJs (recently observed experimentally in Ref. [19]), and it is a consequence of the crossing of the Andreev bound states at zero energy.

We now discuss the spatial dependence of the DOS along the N region. This point is very relevant for two main reasons. From a practical point of view, in order to simulate realistically the differential conductance of a tunnel contact between the weak link and the probe, the DOS needs to be averaged over the contact area (see Sec. V below). From a more fundamental aspect, it is important to understand whether the gapped regions in Fig. 2 are a nonlocal property of the junction, as already proved experimentally for the minigap in two-terminal SNS junctions [29].

Figure 5 shows the dependence of the DOS on x in the left arm, i.e., N_L. Due to the continuity imposed at the S/N interfaces ($x = 1$), the DOS is equal here to its BCS value and there is no modulation with the magnetic flux. Inside the N region, the DOS evolves with a well-defined minigap Δ_w, which is constant in the whole T-shape region. Whereas the minigap is a nonlocal property that can be modulated by the magnetic fluxes, the shape of the DOS for energies larger than the minigap changes along the junction. Notice that for a single flux ($\Phi_R = 0$) the DOS shows two additional peaks at the minigap of the nanowire at energy $\pm\Delta_w$ similar to the edge peaks expected in two-terminal SNS junctions [30].

We finally concentrate on the role of the S/N interface resistances in the energy spectrum of the DOS. These resistances are encoded in the three opacity parameters r_i defined in Eq. (3). The increasing of the opacity of all the interfaces weakens the proximity effect in the JJ, which in turn is reflected in an effective reduction of the minigap [28]. In Fig. 6 we show $N_F(\Phi_L,\Phi_R)$ for different values of r_C and r_R, and by keeping $r_L = 1$. In the symmetric case, $r_R = r_C = 1$, we obtain the symmetric "butterfly" shape observed in Fig. 2 for ideal interfaces. Asymmetries in the interface transparencies lead to an asymmetric configuration of the gapped states in the two-flux space. This asymmetry can be understood by considering three limiting cases: (i) When the right terminal is almost disconnected to the system, $r_R \gg (r_C,r_L)$ (bottom-right plot), Φ_R does not drive the state of the JJ. The latter effectively behaves as a two-terminal junction in which the gapless state is punctual in the flux Φ_L that controls the proximity effect in the junction. (ii) Similarly, when $r_C \gg (r_R,r_L)$ (top left plot), the central terminal is disconnected and the proximity effect in this two-terminal JJ is controlled by the total flux in the interferometer $\Phi_L + \Phi_R$. (iii) When both the interfaces are opaque, $r_R = r_C \gg r_L$ (top right panel), both Φ_L and Φ_R do not drive the proximity effect. In the weak link, a nonmodulated gapped state is induced by the contact with the left S/N interface.

Finally, in Fig. 7 we show how asymmetries affect the evolution of the full energy spectrum of the DOS, in the equal fluxes configuration $\Phi_R = \Phi_L \equiv \Phi$.

This evolution is crucial to clarify the experimental observations reported in Ref. [19] in which the quasiparticle DOSs have been probed by tunneling spectroscopy (see Sec. V for details). One of the main signatures of the three-terminal configuration, with respect to conventional two-terminal JJ, is the conducting gapless state observed for symmetric devices (e.g., at $r_C = r_R = 1$) in a large range of fluxes $\Phi_0/3 < \Phi < 2\Phi_0/3$. In the same range, this conducting state evolves in two additional gapped states by increasing the asymmetries of the interface resistances (e.g., at $r_C = 10^2, r_R = 10$) as also observed in the measurements of asymmetric ω-SQUIPTs [19]. As shown in Fig. 7, these two behaviors are very robust

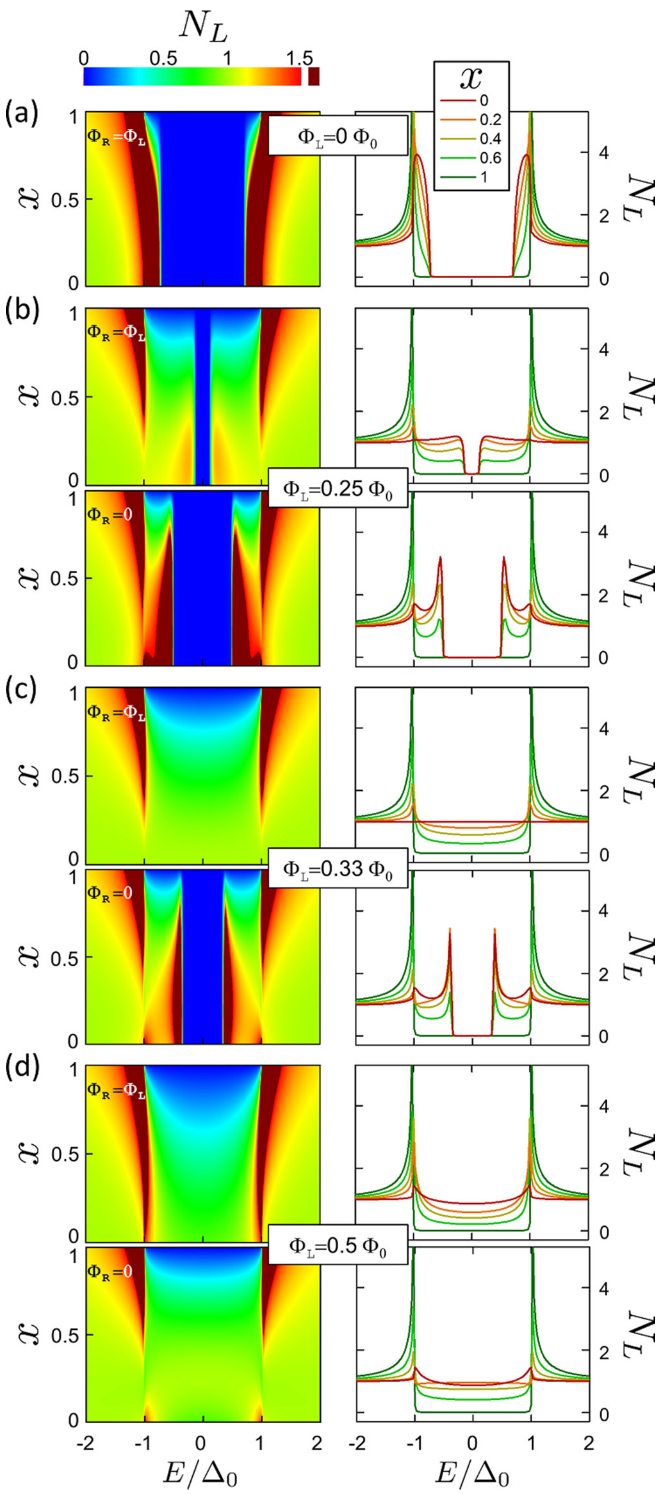

FIG. 5. Spatial dependence of the DOS evaluated at different fluxes, with $E_{\mathrm{Th}}/\Delta_0 = 0.5$ and $\Gamma_S = \Gamma_N = 10^{-3}\Delta_0$. Each central box indicates the value of the flux Φ_L associated with the near plots; the top plots show the case of equal fluxes $\Phi_R = \Phi_L$ and the bottom plots show the single flux case with $\Phi_R = 0$. (a) $\Phi_L = 0$; (b) $\Phi_L = 0.25\Phi_0$; (c) $\Phi_L = 0.33\Phi_0$; and (d) $\Phi_L = 0.5\Phi_0$.

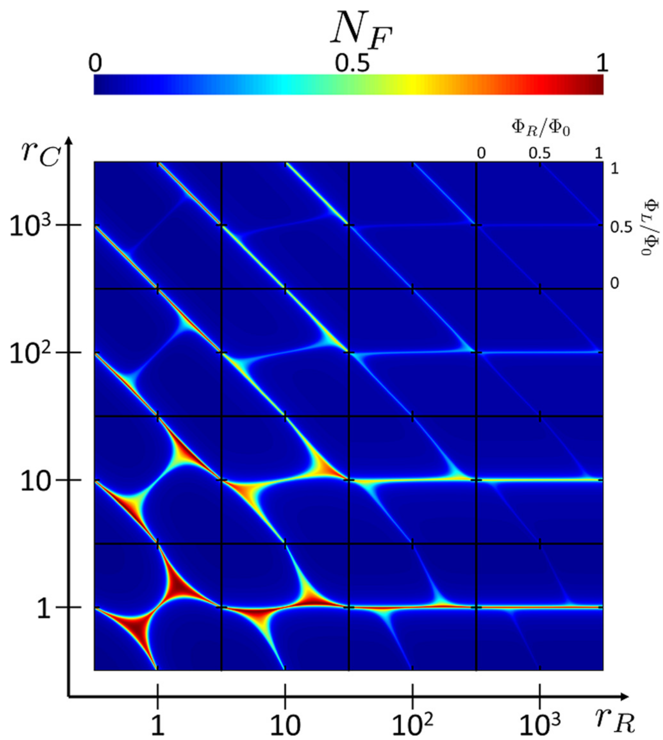

FIG. 6. Evolution of the DOS at the Fermi energy $N_F(\Phi_L,\Phi_R)$ for different values of S/N interface opacities r_R and r_C reported in the x and y axis, respectively. Here $r_L = 1$, $E_{\mathrm{Th}}/\Delta_0 = 0.5$, and $\Gamma_S = \Gamma_N = 10^{-3}\Delta_0$.

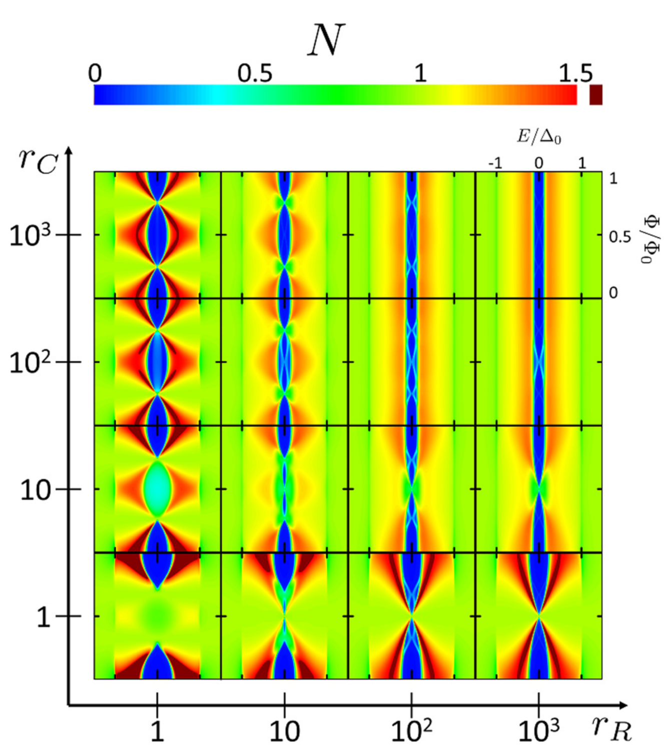

FIG. 7. Energy spectrum of the DOS as a function of equal fluxes $\Phi_L = \Phi_R \equiv \Phi$ and calculated for different values of S/N interface opacity r_R and r_C reported in the x and y axis, respectively. Here $r_L = 1$, $E_{\mathrm{Th}}/\Delta_0 = 0.5$, and $\Gamma_N = \Gamma_S = 10^{-3}\Delta_0$.

and only weakly sensitive to the sample-specific microscopic details of the S/N interface resistances that experimentally can vary also by one order of magnitude. Similar considerations can be drawn also for the fluctuations of the arm lengths affecting only weakly the main features of the DOS (shown in Fig. 6). These show, for example, a closure of the minigap at $\Phi_0/3$ as universal characteristic of the three-terminal geometry.

IV. JOSEPHSON CURRENT

The presence of finite magnetic fluxes Φ_L and Φ_R leads to supercurrents flowing in the proximized metallic nanowire. These supercurrents have a variety of physical behaviors depending on the junction characteristics [31,32]. Within the quasiclassical theory, the supercurrent flowing in the ith arm of the ω-SQUIPT can be written as

$$\mathcal{I}_i = \int_{-\infty}^{+\infty} \tanh\left(\frac{E}{2k_B T}\right) S_i(E)dE, \tag{12}$$

where T is the temperature, k_B is the Boltzmann constant, and $S_i(E)$ is the outgoing spectral supercurrent density in the i arm,

$$\begin{aligned} S_i(E) &= -\frac{G_{N_i}}{4e}\,\mathrm{Re}\{\mathrm{Tr}\{\hat{\tau}_3 \hat{g}_i \partial_x \hat{g}_i\}\} \\ &= \frac{G_{N_i}}{e}\,\mathrm{Re}\left\{\frac{\tilde{\gamma}_i \partial_x \gamma_i - \gamma_i \partial_x \tilde{\gamma}_i}{(1+\gamma_i\tilde{\gamma}_i)^2}\right\}. \end{aligned} \tag{13}$$

In this section, we investigate the outgoing supercurrent flowing through the different arms of the device and its dependence on the magnetic fluxes Φ_R and Φ_L for transparent S/N interfaces. At first, we consider the simple case of equal magnetic fluxes $\Phi_R = \Phi_L \equiv \Phi$. In this case, for symmetry reasons, there is no supercurrent flowing through the central arm $\mathcal{I}_C = 0$, and thus due to current conservation one has $\mathcal{I}_L = -\mathcal{I}_R$. Physically, this means that there is a supercurrent that flows from the right arm to the left one. We analyze this quantity in Fig. 8, showing the supercurrent $\mathcal{I}_L$ and its spectral density $S_L(E)$ for the left arm, at a fixed temperature $T = 0.02T_c$. The supercurrent spectral density $S_L(E)$, present in Fig. 8(a), strongly resembles the quasiparticle DOS, specifying the distribution on energy of Andreev-bound states that carry the supercurrent. In Fig. 8(a), where we plot a representative example with $E_{\mathrm{Th}}/\Delta_0 = 5$, one can see that most of the distribution takes place below the superconducting gap Δ_0. Above it there is an evanescent contribution that brings a counterflowing current, which results in a reduction of the critical current. We note that, for shorter junctions, which correspond to larger values of E_{Th}/Δ_0, the number of states below the superconducting gap increases, giving a greater contribution to supercurrent.

Looking at the color plot in Fig. 8(a) and the energy cuts in Fig. 8(b), a change of sign at all energies is evident for $\Phi/\Phi_0 = 1/3$. This particular value of the flux corresponds exactly to the one in which there is a transition from a gapped to a gapless state in the DOS; see Fig. 4. As for the DOS, this feature does not depend on the junction length. Importantly, this suggests that the supercurrent can be an alternative hallmark of a topological transition in the three-terminal JJ. This characteristic at $\Phi/\Phi_0 = 1/3$ is indeed reflected in the supercurrent $\mathcal{I}_S$, as shown in Fig. 8(c).

To better understand the behavior of $\mathcal{I}_S$, we can consider the simple case in which the Usadel equations (7) can be linearized. Although this is fully justified in the case of a weak

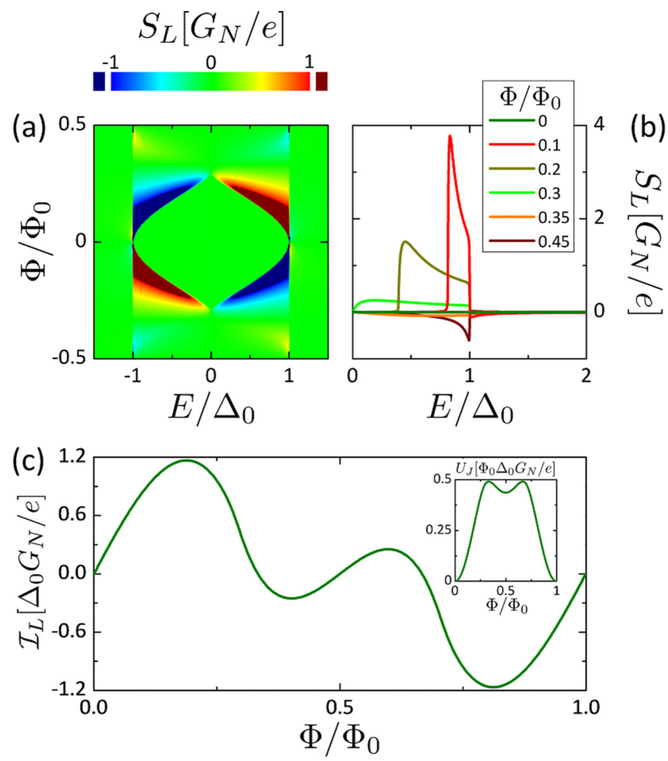

FIG. 8. Outgoing supercurrent of the left arm in the case of equal fluxes $\Phi_R = \Phi_L = \Phi$. (a) Supercurrent spectral density $S_L(E)$ in the case of $E_{\mathrm{Th}}/\Delta_0 = 5$ and with $\Gamma_S = \Gamma_N = 10^{-3}\Delta_0$. Related cuts at different fluxes Φ/Φ_0 are reported in (b). Panel (c) shows the supercurrent $\mathcal{I}_L$ at a fixed temperature $T = 0.02T_C$. $\mathcal{I}_L$ has a periodic behavior as a function of Φ, with nodes due to the three-terminal junction at $\Phi/\Phi_0 = 0$, 1/3, 1/2, and 2/3; see also the cuts present in (b).

proximity effect, with very opaque S/N interfaces ($\tau \ll 1$ and $R_i \gg 1$), it allows for an analytic solution of the system of differential equations (7). As we now discuss, this approach can reproduce most of the qualitative features present in Fig. 8(c). In particular, for equal interfaces and arm lengths, one obtains

$$\mathcal{I}_L = I_0\left[\sin\left(2\pi\frac{2\Phi}{\Phi_0}\right) + \sin\left(2\pi\frac{\Phi}{\Phi_0}\right)\right], \tag{14}$$

where I_0 represents the critical current, whose precise value can be calculated using the linearized Usadel equation [28]. Equation (14) is a periodic function of Φ with period Φ_0, and it presents nodes at $\Phi/\Phi_0 = 0$, 1/3, 1/2, and 2/3. This corresponds to the behavior of the supercurrent shown in Fig. 8, where $\mathcal{I}_L$ is evaluated with a full numerical solution of the Usadel equation (without any weak-proximity assumption). The fact that a linear approach well reproduces most of the qualitative features present in the general case is tightly connected to the three-terminal geometry and to its topological properties. In particular, it indicates that these phase features on the Josephson currents are robust against imperfections and possible microscopic details. It is interesting to notice that, even if in the equal fluxes case there is a supercurrent flow in the side arms and no supercurrent in the central arm, the behavior is not analogous to a two-terminal JJ linked to a loop with a total flux 2Φ. This can be inferred from the additional node present at $\Phi/\Phi_0 = 1/3$. To underline this, we can consider the Josephson energy of the junction U_J. In full analogy with the two-terminal expression, it reads

$$U_J = \frac{\Phi_0}{2\pi}\int \mathcal{I}_L d(\phi_L - \phi_R) = 2\int \mathcal{I}_L d\Phi. \quad (15)$$

This quantity is reported in the inset of Fig. 8(c) for $E_{\mathrm{Th}}/\Delta_0 = 5$. The Josephson energy U_J has two minima at $\Phi/\Phi_0 = 0$ and $1/2$; the global minimum is $\Phi/\Phi_0 = 0$ as in the two-terminal case. The presence of additional local minima is a peculiar feature of the three-terminal JJ and is not present in a two-terminal one. A junction with such a behavior is sometimes called in the literature a $0'$ junction [33,34], due to the presence of metastable states related to the local minima at $\Phi/\Phi_0 = 1/2$. The maximum at $\Phi/\Phi_0 = 1/3$ determines the node present in the supercurrent. The presence of this local minima is a direct consequence of the nontrivial topological configuration, which can be achieved with the ω-SQUIPT and is associated with the presence of the central arm in this three-terminal configuration.

Let us now discuss the case of different fluxes Φ_L and Φ_R and their influence on the ith arm supercurrent. The outgoing supercurrents $\mathcal{I}_L$, $\mathcal{I}_C$, and $\mathcal{I}_R$ are reported in the three panels of Fig. 9 for transparent S/N interfaces and for fixed parameters $E_{\mathrm{Th}}/\Delta_0 = 5$, $\Gamma_N = \Gamma_S = 10^{-3}\Delta_0$, and temperature $T = 0.02T_c$. The dashed line in panel (a) corresponds to the panel (c) in Fig. 8. We immediately note that, in the general case with $\Phi_L \neq \Phi_R$, a finite supercurrent is flowing out of the central arm. As one would expect, the three quantities are not independent, but they are related by current conservation, i.e., $\sum_{i=L,C,R}\mathcal{I}_i = 0$. As before, the qualitative behavior and the main features present in Fig. 9 can be understood inspecting the solution of the linearized Usadel equations. In this case, the supercurrent in each arm is the superposition of the circulating supercurrent in each loop, which gives

$$\begin{aligned}
\mathcal{I}_L &= I_0\left[\sin\left(2\pi\frac{\Phi_L+\Phi_R}{\Phi_0}\right) + \sin\left(2\pi\frac{\Phi_L}{\Phi_0}\right)\right],\\
\mathcal{I}_C &= I_0\left[\sin\left(2\pi\frac{\Phi_R}{\Phi_0}\right) - \sin\left(2\pi\frac{\Phi_L}{\Phi_0}\right)\right],\\
\mathcal{I}_R &= -I_0\left[\sin\left(2\pi\frac{\Phi_L+\Phi_R}{\Phi_0}\right) + \sin\left(2\pi\frac{\Phi_R}{\Phi_0}\right)\right]. \quad (16)
\end{aligned}$$

Again, these simple analytical expressions well reproduce the periodic behavior and the shape of the supercurrents shown in Fig. 9. The full numerical solution extends beyond the linear approximation, which is not able to capture the correct value of the critical current and other details. However, the periodicity and the presence of nodes at precise values of $\Phi_{L,R}/\Phi_0$ are well reproduced by Eq. (16). This fact corroborates the idea that these features are robust in a topological sense and connected to the nontrivial geometry of the three-terminal JJ.

V. MAGNETOMETRIC CHARACTERISTICS OF THE ω-SQUIPT

As shown in Sec. III, the DOS in the junction is modulated by the magnetic fluxes piercing the superconducting loops of the ω-SQUIPT. The transport properties of the quasiparticle in the junction can be tuned from metallic-like (in a gapless state) to insulating-like (in a gapped state). As a consequence, the electrical conduction through the tunnel barrier between the junction and the probe (Fig. 1) is altered [35,36]. This effect allows us to perform magnetometric measurement. In two-terminal SQUIPTs, high sensitivities have been demonstrated [1,5]. In the following, we evaluate the sensitivity of the ω-SQUIPT.

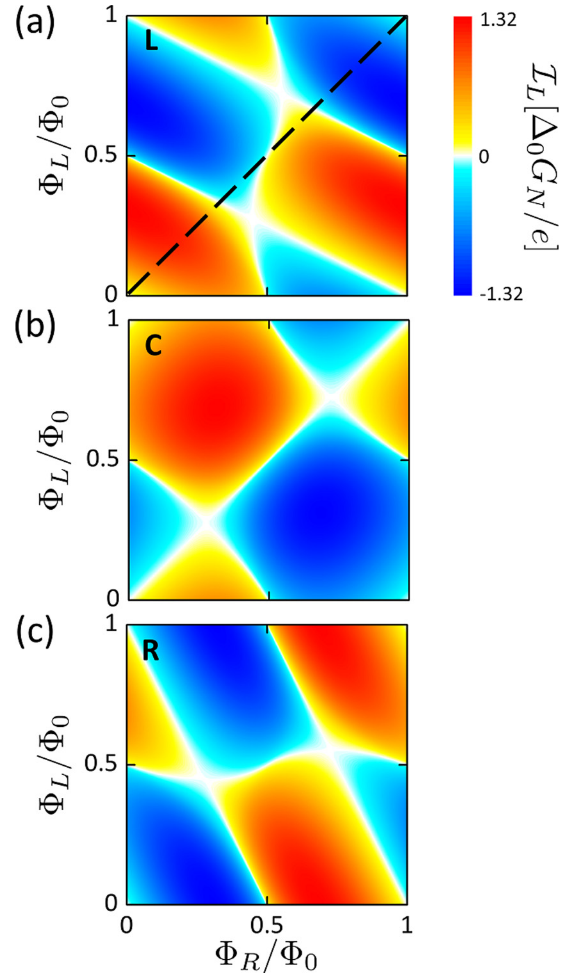

FIG. 9. Color plot of the supercurrents in each arm for different magnetic fluxes Φ_R and Φ_L. Here we have fixed $E_{\mathrm{Th}}/\Delta_0 = 5$ and $\gamma_S = \gamma_N = 10^{-3}\Delta_0$, and $T = 0.02T_c$. The supercurrents flowing out of the left, central, and right arm are plotted in (a), (b), and (c), respectively.

Considering a tunnel probe placed in the middle of the T-shaped N region and covering each arm by a length l_i, the electrical characteristics depend on the spatial average of the local DOS $N_i(x,E,\Phi_L,\Phi_R)$ over the contact area, given by [36]

$$\bar{N}(E,\Phi_L,\Phi_R) \equiv \sum_{i=R,C,L}\frac{1}{w_i}\int_0^{w_i} N_i(x,E,\Phi_L,\Phi_R)dx, \quad (17)$$

where $w_i = l_i/L_i$. By applying a voltage V between the tunnel probe and the junction, a finite tunneling current flows through the contact, whose expression reads

$$I = \frac{1}{eR_t}\int N_P(E-eV)\bar{N}(E)[f_F(E)-f_F(E-eV)]dE, \tag{18}$$

where R_t is the resistance of the tunnel contact, $f_F(E)$ indicates the equilibrium Fermi-Dirac distribution, and $N_P(E)$ is the probe DOS. Like in the usual SQUIPT [1,6], the metallic probe can be made of a normal or superconducting material. These two cases are denoted in the following as normal probe (NP) or superconducting probe (SCP), whose normalized DOSs are, respectively, given by $N_P(E)=1$ and

$$N_P(E) = \left|\mathrm{Re}\,\frac{E+i\Gamma_2}{\sqrt{(E+i\Gamma_2)^2-\Delta_2(T)^2}}\right|. \tag{19}$$

Here Γ_2 and Δ_2 indicate the Dynes parameter and the gap of the superconducting probe. In general, Γ_2 and Δ_2 parameters can be different from those of the ω-SQUIPT described so far. For the sake of simplicity, we assume that $\Gamma_2=\Gamma_S=10^{-4}\Delta_0$ and $\Delta_2=\Delta_0$ and choose $T=0.02T_c$. We consider two symmetric ω-SQUIPTs: one with $E_{\mathrm{Th}}=0.5\Delta_0$ and $w_i=0.2$, and a second one with $E_{\mathrm{Th}}=5\Delta_0$ and $w_i=0.68$ for $i=L,R,C$. For an Al-Cu–based device, these parameters correspond to $L_i\approx 90$ nm and $L_i\approx 30$ nm, respectively, and a contact length in each arm $l_i\approx 20$ nm. All these values are achievable with state-of-the-art nanofabrication techniques [5,37].

Figure 10 shows the current-voltage (I-V) characteristic in linear and logarithmic scale for fluxes Φ. Panels (a) and (b) refer to the NP case, while panels (c) and (d) refer to SCP. The main modulation in the I-V characteristic happens in the flux interval $\Phi/\Phi_0=[0,1/3]$, for which the weak link is in the gapped state. The main differences between the NP and SCP is the presence in the latter of a permanent voltage gap and peaks due to the superconducting probe. The Y-logarithmic plots on the right column give a clearer insight on the modulation properties. The I-V characteristics are modulated in a voltage range of Δ_w/e corresponding to a swing in current of a few orders of magnitude that can further increase by lowering Γ.

Considering an electrical setup where the ω-SQUIPT is biased with a proper current I_b, the voltage drop depends on flux, giving the flux to voltage characteristics $V(\Phi)$ (see Fig. 1). The optimal voltage-gap swing Δ_w/e can be approached at low current bias, making the ω-SQUIPT a low power dissipation magnetometer. In Fig. 11 on the left side, the flux to voltage characteristics $V(\Phi)$ is plotted for two representative devices with $E_{\mathrm{Th}}/\Delta_0=0.5$ and 5 in the case of both NP and SCP. The main modulation interval is $\Phi/\Phi_0=[-1/3,1/3]$ (with Φ_0 periodicity); on the contrary, the interval $\Phi/\Phi_0=[2/3,4/3]$ has a flat trend. The performance of the device as a magnetometer can be estimated by the flux to voltage transfer function

$$\mathcal{F}(\Phi)=\frac{\partial V_I}{\partial \Phi}. \tag{20}$$

The $\mathcal{F}$ function is reported in Fig. 11 on the right side. The performance in terms of magnetometry of the ω-SQUIPT is $3.8\Delta_0/e\Phi_0$ for $E_{\mathrm{Th}}/\Delta_0=0.5$ and $4.3\Delta_0/e\Phi_0$ for $E_{\mathrm{Th}}/\Delta_0=5$.

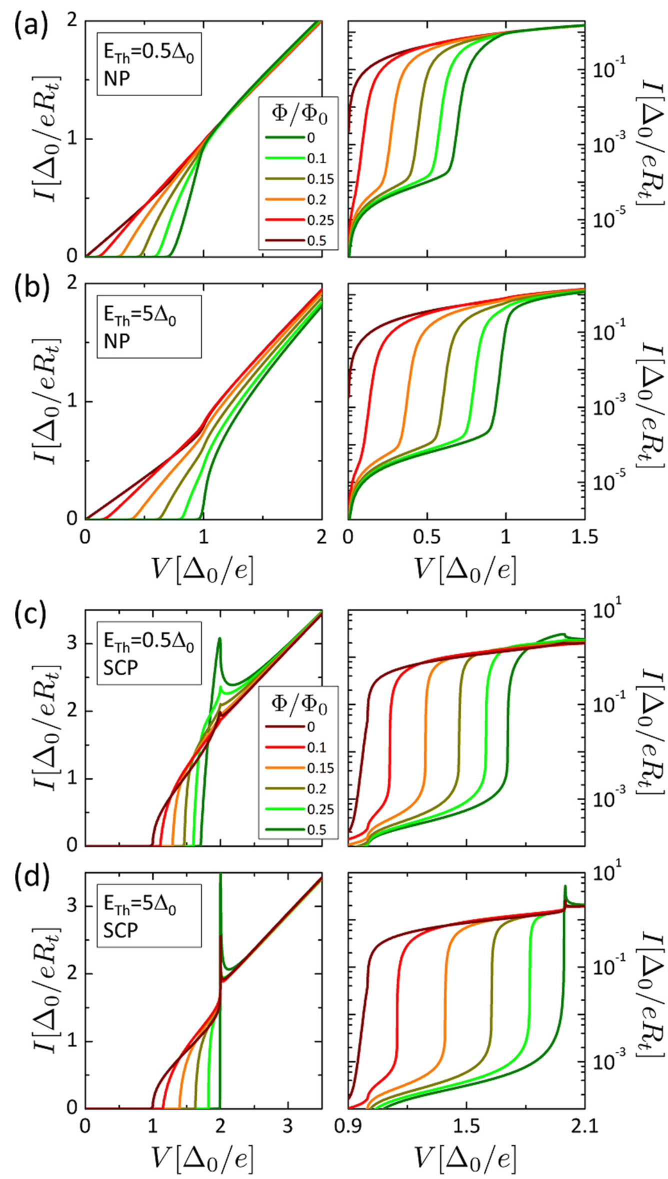

FIG. 10. I-V characteristics of the tunnel contact between the probe and the ω-SQUIPT junction at different values of flux Φ, with ideal S/N interfaces. Here, $\Gamma_S=\Gamma_N=10^{-4}\Delta_0$. This quantity is reported both in linear (left column) and Log y (right column) scale. Panels (a) and (b) refer to the ω-SQUIPT with a normal metallic probe NP and $E_{\mathrm{Th}}/\Delta_0=0.5$ and 5, respectively. Panels (c) and (d) refer to the ω-SQUIPT with a superconducting probe SCP and $E_{\mathrm{Th}}/\Delta_0=0.5$ and 5, respectively.

We note that these performances are lower than those of a conventional SQUIPT. Indeed, for the sake of comparison, it is sufficient to consider the total flux on the device. The total flux interval of the main modulation is from zero to the closure of the induced minigap. In the SQUIPT, the minigap closes at $\Phi_0/2$; in a ω-SQUIPT, the gap closes at total flux $2\Phi_0/3$, which is greater than the SQUIPT case. This means that a certain swing in the output signal requires a greater flux variation in the ω-SQUIPT, thus lowering its sensitivity.

Nevertheless, the ω-SQUIPT has also interesting gradiometric properties. Let us consider the region around the

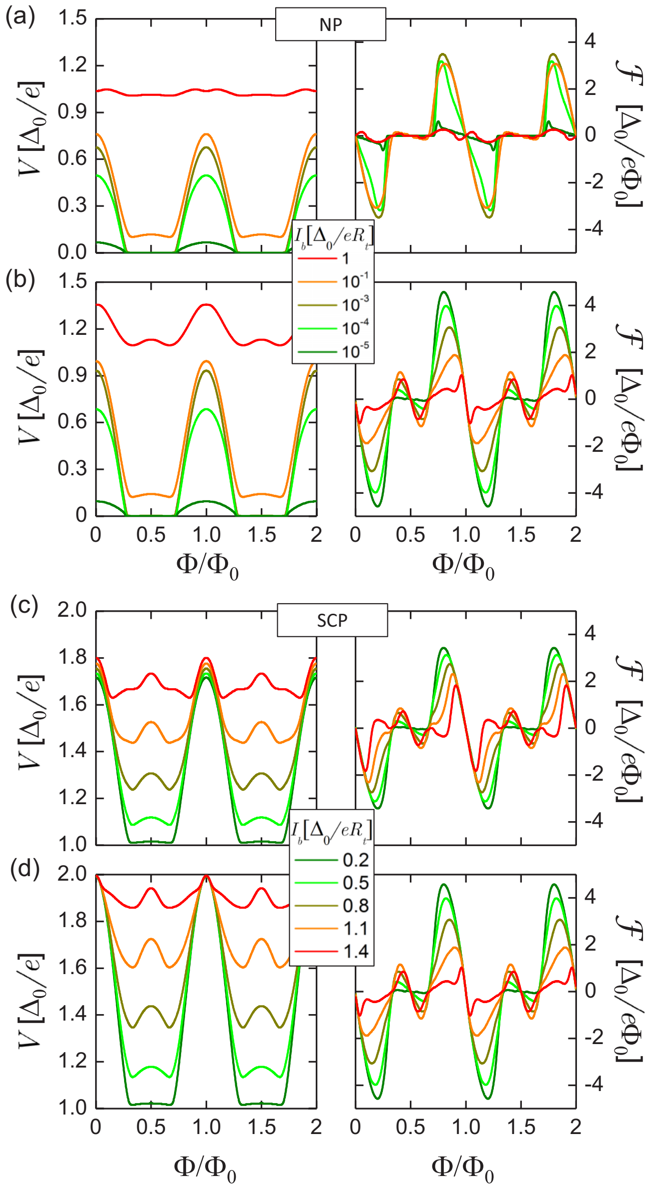

FIG. 11. Left column: Flux to voltage characteristic $V_I(\Phi)$ of the ω-SQUIPT. Right column: Transfer function $\mathcal{F}$ associated with the flux voltage characteristics. Here, the S/N interfaces are transparent and $\Gamma_S = \Gamma_N = 10^{-4}\Delta_0$. Parts (a) and (b) correspond to the case of ω-SQUIPT with a normal probe NP and $E_{\mathrm{Th}}/\Delta_0 = 0.5$ and 5, respectively. Parts (c) and (d) refer to the ω-SQUIPT with a superconducting probe SCP and $E_{\mathrm{Th}}/\Delta_0 = 0.5$ and 5, respectively.

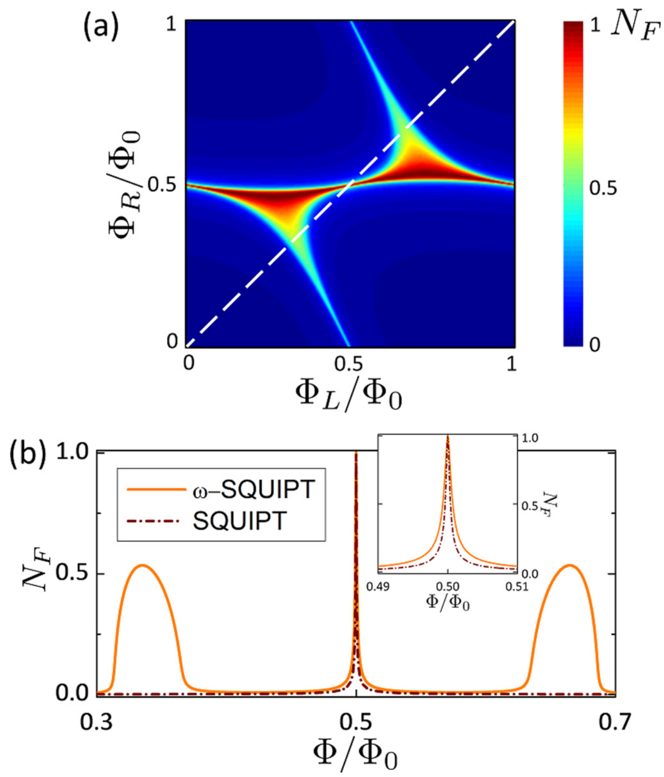

FIG. 12. Working principle of the ω-SQUIPT as a magnetometer. Here the interfaces are asymmetric, with $r_R = r_C = 0.1$ and $r_L = 5$. Panel (a) presents the DOS at Fermi energy N_F as a function of Φ_L and Φ_R. Panel (b) shows the DOS of the ω-SQUIPT at Fermi energy N_F in the case of equal fluxes $\Phi_L = \Phi_R = \Phi$ (orange solid line). For the sake of comparison, we plot also the result in the case of a conventional two-terminal device (dark red dashed curve) with equal contact resistances $r = 0.1$.

fluxes point $(\Phi_L/\Phi_0, \Phi_R/\Phi_0) = (1/2, 1/2)$ in the N_F plot for full symmetric ω-SQUIPT (Fig. 2). Along the diagonal line, $\Phi_L = \Phi_R$, the modulation is smaller with respect to other directions. In particular, it reaches the maximum value for $\Phi_L = -\Phi_R$. Hence, the sensitivity is greater for magnetic fields with a spatial gradient. Gradiometric properties are exploited for magnetic measurement protected from noise caused by a far source [38].

Finally, we comment on a different possible application of the ω-SQUIPT as a magnetometer. Basically, this possibility relies on the shape of the DOS at Fermi energy of the three-terminal JJ. Consider, for example, an ω-SQUIPT whose S/N resistances are asymmetric with $r_R = r_C = 0.1$ and $r_L = 5$, as in Fig. 12. In this case, the shape of the DOS at Fermi energy N_F is skewed (Fig. 12). A symmetric flux that goes from $\Phi = 0$ to $\Phi = \Phi_0$ [Fig. 12, white line in panel (a)] crosses the red conductive region in three different points. In these crossing points, the DOS at Fermi energy shows peaks depending on the flux Φ. The strong modulation of N_F can be exploited for magnetometry. Notice that here, the experimental setup should be different from the current biased setup discussed above. For example, a lock-in configuration that measures the differential conductance at zero voltage can be used. Panel (b) of Fig. 12 shows the cuts of the DOS at the Fermi energy for equal fluxes in the asymmetric configuration with $r_R = r_C = 0.1$ and $r_L = 5$ (orange solid line). For the sake of comparison, we have also plotted the analogous quantity for a conventional SQUIPT [6] with opacities $r = 0.1$ (dark red dashed curve). As one can argue from the figure, also the two-terminal device can be used as a magnetometer, since it presents a peaked structure around $\Phi = \Phi_0/2$ [6]. The inset depicts a magnification in the region near $\Phi = \Phi_0/2$, showing that the peak is sharper in the case of a conventional SQUIPT. Nevertheless, the ω-SQUIPT has also other intervals of modulation in $\Phi = (0.34 \pm 0.03)\Phi_0$ and $\Phi = (0.66 \pm 0.03)\Phi_0$, demonstrating that it has a larger region of working points as a magnetometer.

VI. CONCLUSIONS

In summary, the paper reports an exhaustive theoretical investigation of different coherent transport properties of a three-terminal hybrid device, the so-called ω-SQUIPT. By means of a full numerical solution of the Usadel equation, extended to the case of three S leads, we have studied the effects on the proximized metallic nanowire of the length, the inelastic scattering, and the quality of the S/N interfaces. We have shown that the spectral properties are a useful tool to identify transitions between gapless and gapped states in this three-terminal setup. The induced supercurrents in the different arms of the device are discussed in detail, showing that these can be an alternative hallmark of nontrivial topological properties. The quasiparticle transport properties through a metallic probe tunnel-coupled to the Josephson junction are presented both in the case of a metallic and a superconducting probe. Since the ω-SQUIPT is sensitive to magnetic fluxes, we have inspected its magnetometric features, finding that this device can have potential applications as a gradiometer or magnetometer. Finally, we emphasize that the theoretical results reported here can serve as a starting point for a better fundamental understanding of multiterminal JJs, which recently have drawn great interest due to their exotic properties and potential applications in quantum computing.

ACKNOWLEDGMENTS

F.V. and F.G. acknowledge the European Research Council under the European Union's Seventh Framework Program (FP7/2007-2013)/ERC Grant Agreement No. 615187-COMANCHE and MIUR-FIRB2013—Project Coca (Grant No. RBFR1379UX) for partial financial support. The work of E.S. was funded by a Marie Curie Individual Fellowship (MSCA-IFEF-ST No. 660532-SuperMag). The work of F.S.B. was supported by Spanish Ministerio de Economia y Competitividad (MINECO) through Project No. FIS2014-55987-P.

[1] F. Giazotto, J. T. Peltonen, M. Meschke, and J. P. Pekola, Nat. Phys. **6**, 254 (2010).
[2] W. L. McMillan, Phys. Rev. **175**, 537 (1968).
[3] K. D. Usadel, Phys. Rev. Lett. **25**, 507 (1970).
[4] E. Strambini, F. S. Bergeret, and F. Giazotto, Appl. Phys. Lett. **105**, 082601 (2014).
[5] A. Ronzani, C. Altimiras, and F. Giazotto, Phys. Rev. Appl. **2**, 024005 (2014).
[6] S. D'Ambrosio, M. Meissner, C. Blanc, A. Ronzani, and F. Giazotto, Appl. Phys. Lett. **107**, 113110 (2015).
[7] M. Meschke, J. T. Peltonen, J. P. Pekola, and F. Giazotto, Phys. Rev. B **84**, 214514 (2011).
[8] P. Virtanen, A. Ronzani, and F. Giazotto, Phys. Rev. Appl. **6**, 054002 (2016).
[9] F. Giazotto and F. Taddei, Phys. Rev. B **84**, 214502 (2011).
[10] C. Padurariu, T. Jonckheere, J. Rech, R. Mélin, D. Feinberg, T. Martin, and Yu. V. Nazarov, Phys. Rev. B **92**, 205409 (2015).
[11] T. Yokoyama and Y. V. Nazarov, Phys. Rev. B **92**, 155437 (2015).
[12] R.-P. Riwar, M. Houzet, J. S. Meyer, and Y. V. Nazarov, Nature Commun. **7** 11167 (2016).
[13] E. Eriksson, R.-P. Riwar, M. Houzet, J. S. Meyer, and Yu. V. Nazarov, arXiv:1612.05418.
[14] S. Mai, E. Kandelaki, A. Volkov, and K. Efetov, Phys. Rev. B **87**, 024507 (2013).
[15] M. H. S. Amin, A. N. Omelyanchouk, and A. M. Zagoskin, J. Low Temp. Phys. **27**, 616 (2001).
[16] B. van Heck, S. Mi, and A. R. Akhmerov, Phys. Rev. B **90**, 155450 (2014).
[17] M. H. S. Amin, A. N. Omelyanchouk, A. Blais, A. Massen van den Brink, G. Rose, T. Duty, and A. M. Zagoskin, Physica C **368**, 310 (2002).
[18] M. Alidoust, G. Sewell, and J. Linder, Phys. Rev. B **85**, 144520 (2012).
[19] E. Strambini, S. D'Ambrosio, F. Vischi, F. S. Bergeret, Y. V. Nazarov, and F. Giazotto, Nature Nanotechnol. **11** 1055 (2016).
[20] W. Belzig, F. K. Wilhelm, C. Bruder, G. Schn, and A. D. Zaikin, Superlattices Microstruct. **25**, 1251 (1999).
[21] J. W. Serene and D. Rainer, Phys. Rep. **101**, 221 (1983).
[22] Y. V. Nazarov, Superlattices Microstruct. **25**, 1221 (1999).
[23] Y. Nazarov and Y. Blanter, *Quantum Transport: Introduction to Nanoscience* (Cambridge University Press, Cambridge, 2009).
[24] K.-H. Bennemann and J. B. Ketterson, *Superconductivity* (Springer-Verlag, Berlin, 2008), Vol. I.
[25] R. C. Dynes, V. Narayanamurti, and J. P. Garno, Phys. Rev. Lett. **41**, 1509 (1978).
[26] J. P. Pekola, V. F. Maisi, S. Kafanov, N. Chekurov, A. Kemppinen, Y. A. Pashkin, O.-P. Saira, M. Möttönen, and J. S. Tsai, Phys. Rev. Lett. **105**, 026803 (2010).
[27] M. Amundsen, J. A. Ouassou, and J. Linder, Sci. Rep. **7**, 40578 (2017).
[28] J. C. Hammer, J. C. Cuevas, F. S. Bergeret, and W. Belzig, Phys. Rev. B **76**, 064514 (2007).
[29] H. le Sueur, P. Joyez, H. Pothier, C. Urbina, and D. Esteve, Phys. Rev. Lett. **100**, 197002 (2008).
[30] F. Zhou, P. Charlat, B. Spivak, and B. Pannetier, J. Low Temp. Phys. **110**, 841 (1998).
[31] A. A. Golubov, M. Y. Kupriyanov, and E. Il'ichev, Rev. Mod. Phys. **76**, 411 (2004).
[32] K. K. Likharev, Rev. Mod. Phys. **51**, 101 (1979).
[33] A. V. Rozhkov and D. P. Arovas, Phys. Rev. B **62**, 6687 (2000).
[34] A. V. Rozhkov and D. P. Arovas, Phys. Rev. Lett. **82**, 2788 (1999).
[35] I. Giaever, Phys. Rev. Lett. **5**, 147 (1960).
[36] M. Tinkham, Phys. Rev. B **6**, 1747 (1972).
[37] H. Rabani, F. Taddei, F. Giazotto, and R. Fazio, J. Appl. Phys. **105**, 093904 (2009).
[38] J. Clarke and A. Braginski, *The SQUID Handbook: Fundamentals and Technology of SQUIDs and SQUID Systems* (Wiley-VCH, Weinheim, 2006).